iScience

CellPress
OPEN ACCESS

Article

Ion-selective solar crystallizer with rivulets

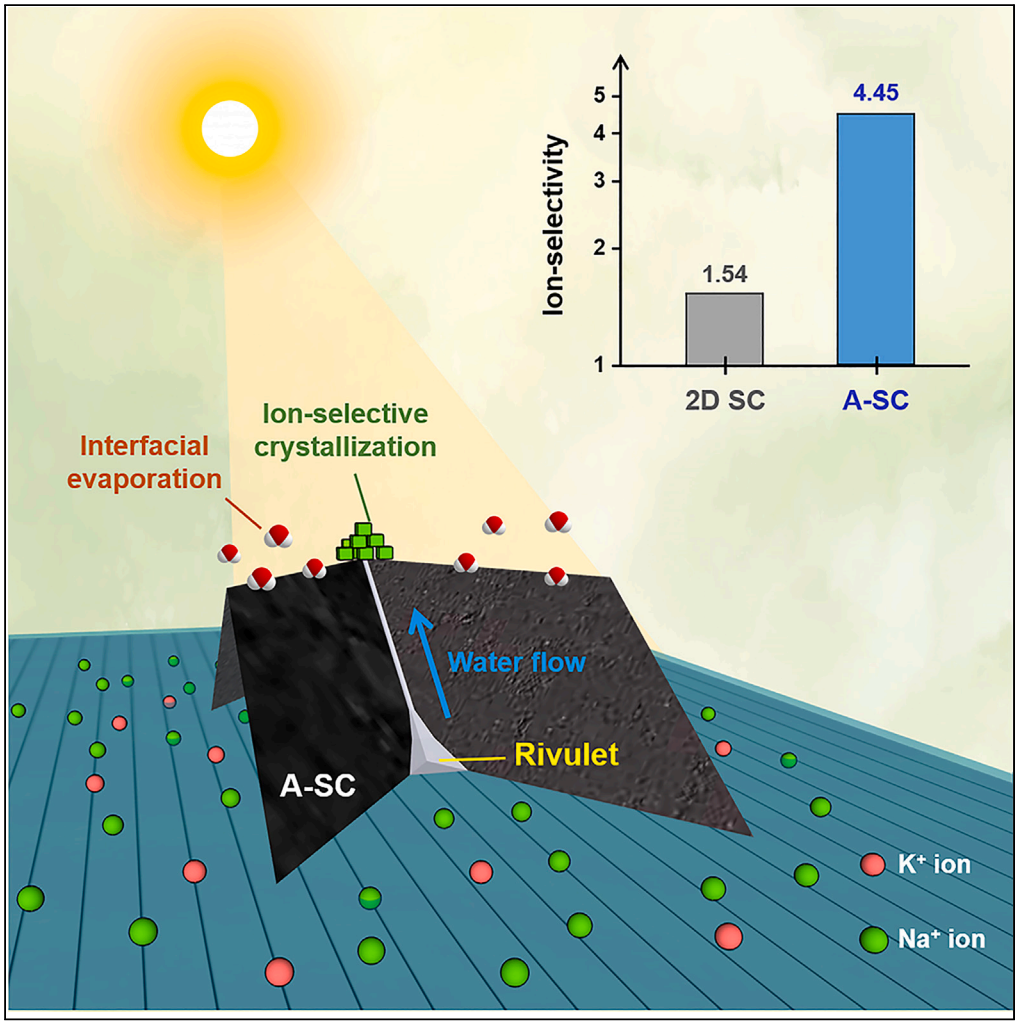

Jihun Choi,
Jaehyun Na,
Sangmin Jeon

jeons@postech.ac.kr

Highlights

The first-ever ion-selective solar crystallizer is developed

The V-shaped structure creates rivulets that facilitate solution transport

High evaporation rate (1.51 kg/m^{2}h) and ion-selectivity (4.45) are achieved

Choi et al., iScience 26, 106926
June 16, 2023
https://doi.org/10.1016/j.isci.2023.106926

iScience

CellPress
OPEN ACCESS

Article

Ion-selective solar crystallizer with rivulets

Jihun Choi,[1] Jaehyun Na,[1] and Sangmin Jeon[1,2,*]

SUMMARY

Bulk evaporation of brine is a sustainable method to obtain minerals with the inherent advantage of selective crystallization based on ion solubility differences, but it has a critical drawback of requiring a prolonged time period. In contrast, solar crystallizers based on interfacial evaporation can reduce the processing time, but their ion-selectivity may be limited due to insufficient re-dissolution and crystallization processes. This study presents the first-ever development of an ion-selective solar crystallizer featuring an asymmetrically corrugated structure (A-SC). The asymmetric mountain structure of A-SC creates V-shaped rivulets that facilitate solution transport, promoting not only evaporation but also the re-dissolution of salt formed on the mountain peaks. When A-SC was employed to evaporate a solution containing a mixture of Na^+ and K^+ ions, the evaporation rate was 1.51 kg/m^{2}h and the relative concentration of Na^+ to K^+ in the crystallized salt was 4.45 times higher than that in the initial solution.

INTRODUCTION

Seawater is a promising source of various minerals such as sodium, magnesium, potassium, and lithium compounds, and has been mined for thousands of years.[1,2] Compared to traditional land-based mining, seawater mining poses reduced environmental and health risks, making it a viable alternative.[3,4] However, the low salt concentrations in seawater make it an expensive and energy-intensive process, which has hindered its widespread adoption. This challenge can be addressed by using seawater brines with higher salt concentrations, which can be obtained from expanding desalination plants.[5,6]

Of the various technologies available for brine mining, solar evaporation stands out as the most sustainable option because it harnesses abundant solar energy and enables selective enrichment of salts based on the solubility differences of each ion.[3,5] However, traditional solar evaporation relies on bulk evaporation, which is slow because of low light absorbance and high heat dissipation.[7,8] Previous efforts to improve the solar evaporation efficiency have focused primarily on increasing light absorbance, such as adding a black layer to the bottom of an evaporating pond,[9] integrating a heat exchange system with a solar thermal pond,[10] or incorporating light-absorbing nanoparticles into the solution,[11] but have not fully addressed the issue of high heat dissipation in bulk solutions.

The utilization of a modern solar steam generator (SSG), which is based on interfacial evaporation at the solid surface where the seawater or brine meets air, can effectively minimize heat dissipation during evaporation. SSG is constructed using a solid material with highly efficient photothermal properties that absorb solar energy and thermal insulating properties that prevent heat loss into the bulk solution.[12–14] In addition, SSG possesses high water transport properties that enable the efficient spreading of water to the entire surface. However, the primary focus of SSG is not on the production of salt, but rather on the production of fresh water. As a result, significant efforts have been made to prevent salt precipitation during evaporation.[15–18]

In contrast, a solar crystallizer (SC), a variation of SSG, is primarily designed for the production of salts.[19–21] When extracting salt from seawater or brine using SCs, two challenges are encountered: the reduction of water evaporation because of the accumulation of salt on the evaporating surface, and low ion-selectivity in the crystallized salt because of inadequate re-dissolution and crystallization processes. Wang et al. separated the crystallizing surface from the light absorbing surface to prevent the reduction of water evaporation because of salt buildup.[22] Zhang et al. were able to prevent salt buildup on the evaporating surface by confining the crystallization process to the edge of the evaporator.[23] Moreover, several efforts have been made to improve the energy efficiency and evaporation performance of SCs by integrating them with

[1]Department of Chemical Engineering, Pohang University of Science and Technology (POSTECH), Pohang, Gyeongbuk, Republic of Korea

[2]Lead contact

*Correspondence: jeons@postech.ac.kr

https://doi.org/10.1016/j.isci.2023.106926

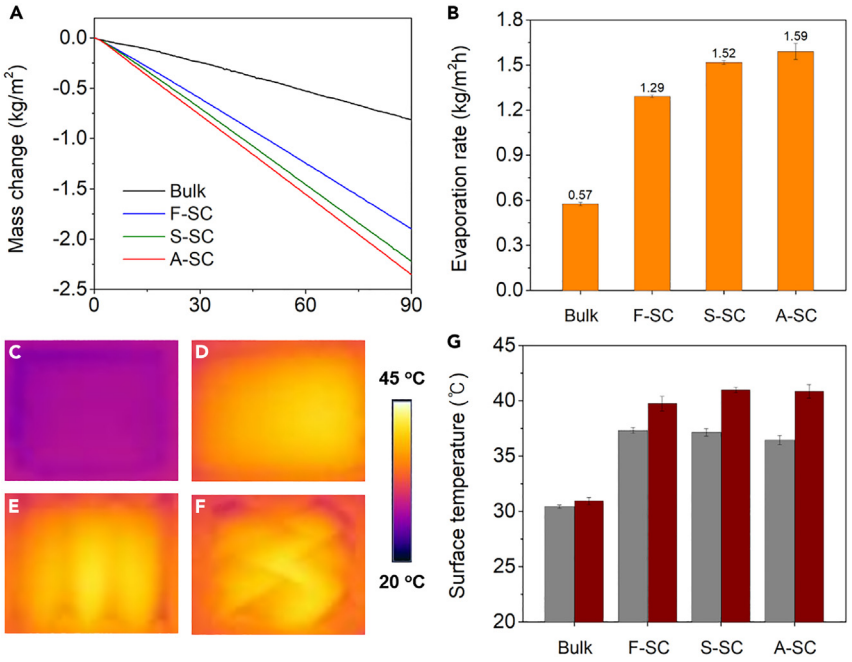

Figure 1. Improved water evaporation performance with SCs

(A) Evaporation-induced mass changes of water without the use of SC (black, bulk evaporation), with the use of F-SC (blue), S-SC (green) and A-SC (red).

(B) Water evaporation rates with and without the use of SC.

IR images of the surfaces of (C) bulk water, (D) F-SC, (E) S-SC, and (F) A-SC after 1.5 h evaporation under 1 sun illumination.

(G) Average (gray) and maximum (wine) surface temperature of each SC after 1.5 h evaporation under 1 sun illumination.

Data are represented as mean ± SD.

multistage passive distillers,[24] photovoltaic systems,[25] or precipitation processes.[26] However, previous studies solely focused on the removal or production of total salts with no investigation into ion-selective crystallization.

In this study, to the best of our knowledge, we conducted the first investigation into the ion-selectivity of SC using three SCs with distinct structures: a flat SC (F-SC), a symmetrically corrugated SC (S-SC) with a parallel pattern, and an asymmetrically corrugated SC (A-SC) with a herringbone tessellation pattern. Although A-SC has been previously used as SSG,[27] its ion-selective characteristics as SC and the advantages of its asymmetrical structure have yet to be explored. When each SC was employed to evaporate a solution containing a mixture of Na^+ and K^+ ions, the salt produced from A-SC exhibited the highest ion-selectivity. This result was attributed to the facilitated flow through V-shaped rivulets of solution, which improved re-dissolution and crystallization processes.

RESULTS AND DISCUSSION

Improved water evaporation performance with SCs

Figure 1A shows the evaporation-induced mass changes of water under different conditions, including without the use of SC (i.e., bulk evaporation), and with the use of F-SC, S-SC or A-SC. The linear decrease in mass indicates that the measurement was conducted under steady-state conditions. The steady-state evaporation rate was calculated by dividing the mass change per hour by the sample's projected area (Figure 1B). With the use of F-SC, the evaporation rate increased from 0.57 kg/m^{2}h (bulk evaporation) to 1.29 kg/m^{2}h, because of improved light absorption efficiency and reduced heat loss into the bulk solution. Both S-SC and A-SC exhibited enhanced dark evaporation because of their 3D structures, resulting in an increased evaporation rate of 1.52 kg/m^{2}h and 1.59 kg/m^{2}h, respectively. The slightly higher evaporation rate of A-SC compared to S-SC can be attributed to the wider gap between the mountain folds of A-SC (10 mm) compared to S-SC (5 mm), which increased dark evaporation by preventing vapor accumulation.[28] The evaporation rate of A-SC represents a 2.8-fold increase compared to bulk evaporation. Figures 1C–1F

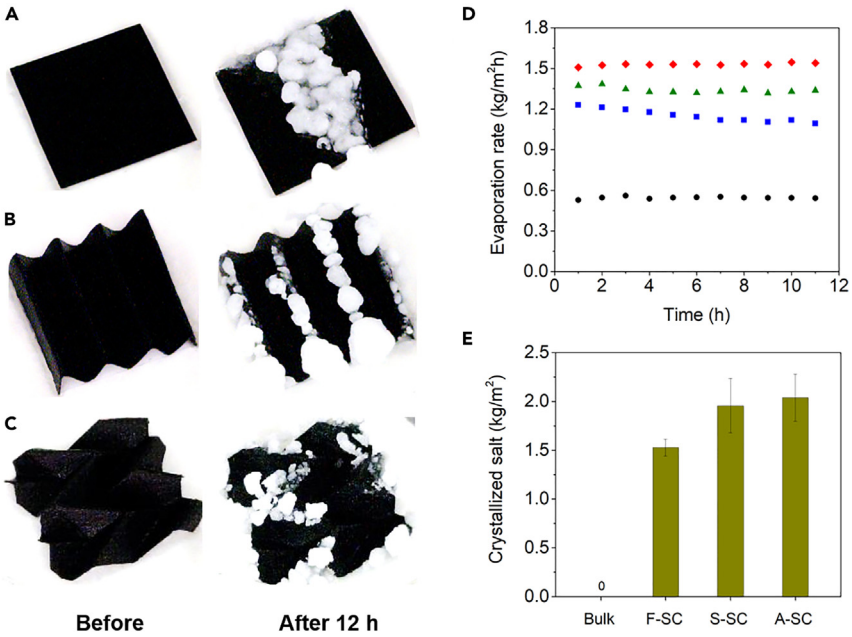

Figure 2. Brine evaporation and salt crystallization with SCs

Photos of (A) F-SC, (B) S-SC and (C) A-SC before (left panel) and after (right panel) evaporation for 12 h.

(D) Time-dependent changes of evaporation rate of bulk evaporation (black circle), with the use of F-SC (blue square), S-SC (green triangle) and A-SC (red diamond).

(E) Mass of the crystallized salt obtained after evaporation for 12 h from each sample. Data are represented as mean ± SD.

show IR images of the surface temperatures of bulk water (without SC), F-SC, S-SC, and A-SC in water, respectively. The average and maximum surface temperature of each SC after 1.5 h of evaporation under 1 sun illumination are displayed in Figure 1G. The average surface temperature of bulk water (30 °C) was lower than that of F-SC (37 °C), confirming that F-SC had higher light absorption efficiency than water. It is worth noting that the average surface temperature in the mountain folds of A-SC (36 °C) was lower than that in the valley folds (40 °C) because of evaporation-induced cooling, indicating that more water evaporates in the mountain folds. In addition, this temperature difference creates a thermocapillary force, inducing a Marangoni flow from the valley folds to the mountain folds.[29,30]

Brine evaporation and salt crystallization with SCs

To evaluate the performance of SCs for evaporation and selective crystallization, brine was evaporated with each SC. Because seawater did not produce salt precipitation within a daily cycle because of its low salt concentration (Figure S1), a solution containing NaCl and KCl was used as a representative sample of brines with higher salt concentration, such as brines found in salt lakes or desalination plant concentrates. The mass ratio of Na^+ to K^+ ions in the solution ($R_{solution}$) was measured to be 4.19, which is similar to that of brine from salt lakes (e.g., Salar de Atacama) or bittern from salt farms.[31,32] No crystallized salts were observed from the bulk solution after 12 h of evaporation, indicating that neither Na^+ nor K^+ ions were saturated. A control experiment showed that salt production from the 20 mL solution via bulk evaporation took 63 h to initiate (Figure S2A). In contrast, utilizing SCs resulted in salt crystallization in only 1–2 h (Figures S2B–S2D), with substantial accumulation after 12 h. These results demonstrate that SCs can generate salt products in daily cycles, whereas bulk evaporation requires a significantly longer period.

The photo in Figure 2A shows the salts that have crystallized on F-SC. Note that the salts predominantly crystallized on the middle region of F-SC, whereas the left and right sections had no salt presence. This is because of the continuous supply of the solution to these regions through the underlying FP wick shaped like a desk (Scheme 1A). In contrast to F-SC, salts mainly crystallized on the mountain folds of S-SC and A-SC as shown in Figures 2B and 2C, despite evaporation occurring across their entire surface. This suggests that the concentration of the solution on the side surfaces remains below the saturation

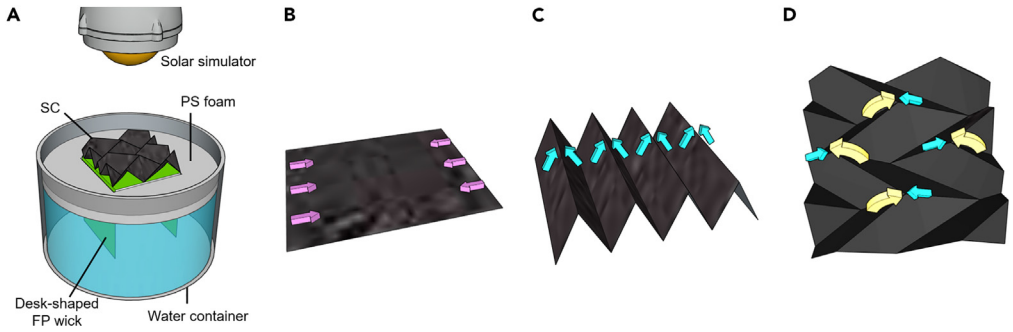

Scheme 1. Experimental setup and schematic of SCs

(A) Experimental setup. Schematic of (B) F-SC, (C) S-SC, and (D) A-SC. The direction and size of the arrows represent both the direction and relative amount of the solution flow.

concentration, whereas it exceeds the saturation concentration in the mountain folds.[33] This position-dependent concentration difference results in the generation of an upward Marangoni flow, which works in conjunction with the Marangoni flow induced by the temperature gradient. This combined flow can effectively transport the solution from the valley folds to the mountain folds at rates of order of 10^{-4} to 10^{-2} m/s.[34–36]

Figure 2D shows the temporal variation in the evaporation rate of each sample. The evaporation rate of bulk solution remained nearly constant (0.55 kg/m^{2}h) during evaporation for 12 h. The evaporation rate with F-SC (1.15 kg/m^{2}h) was higher than that of bulk evaporation but decreased over time because of extensive crystallization of the salt, which interfered with light absorption. On the other hand, the evaporation rates with S-SC (1.34 kg/m^{2}h) and A-SC (1.51 kg/m^{2}h) were higher than that with F-SC, owing to their 3D structures which enhanced dark evaporation. The evaporation rates with S-SC and A-SC exhibited little decrease over time, partly because localized crystallization minimized the light absorption blockage, and partly because the presence of gaps in the salt crystals facilitated solution transport and acted as an additional evaporation surface (Figure S3).[26] Figure 2E shows the quantity of crystallized salt produced after 12 h of solar evaporation for each sample. As previously stated, bulk evaporation did not yield any salt, whereas F-SC resulted in the production of 1.53 kg/m^2 of crystallized salt. S-SC (1.96 kg/m^2) and A-SC (2.04 kg/m^2) produced a larger amount of crystallized salt because of their higher evaporation rates. Although the amounts of the crystallized salts from S-SC and A-SC are similar, the ion composition in the salts differs significantly.

Ion-selective crystallization facilitated by A-SC

The crystallized salts collected from bulk evaporation, F-SC, S-SC, and A-SC were subjected to ion chromatography analysis to determine their ionic composition. The selectivity of Na^+ to K^+ ($S_{Na/K}$) was calculated by dividing the mass ratio of Na^+ to K^+ in the crystallized salt (R_{salt}) by that of initial solution ($R_{solution}$ = 4.19). Through bulk evaporation, the R_{salt} was found to be 21.26 (Figure S4), which indicates that the relative concentration of Na^+ to K^+ in the crystallized salt was 5.07 times greater than that in the initial solution (i.e., $S_{Na/K}$ = 5.07). This ion-selectivity is markedly higher than that achieved using F-SC ($S_{Na/K}$ = 1.54) or S-SC ($S_{Na/K}$ = 2.62). It is worth noting that, despite the inherent disadvantage of requiring a longer time period, bulk evaporation exhibits high ion-selectivity. This is because the slow bulk evaporation process allows a sufficient time for re-dissolution and crystallization to occur, resulting in an equilibrium composition that is determined by the difference in SI values.[37]

Figure 3A shows the relationship between the simulated saturation index (SI) of NaCl and KCl and the amount of water evaporated from a solution containing 10 wt % NaCl and 2 wt % KCl. When the SI value is positive, salt crystallization can occur. At a water evaporation level of 76%, the SI value of NaCl becomes positive, whereas the SI value of KCl remains highly negative, suggesting a preference for NaCl crystallization at this level of evaporation. This prediction is consistent with the experimental findings that salt crystallization during bulk evaporation began at 73% water evaporation, and that 96% of the resulting crystals were composed of NaCl.

Figure 3B shows the selectivity of Na^+ to K^+ in the crystallized salts produced from F-SC, S-SC, and A-SC after 12 h of solar crystallization. The ion-selectivity of F-SC was found to be low at 1.54, indicating that the

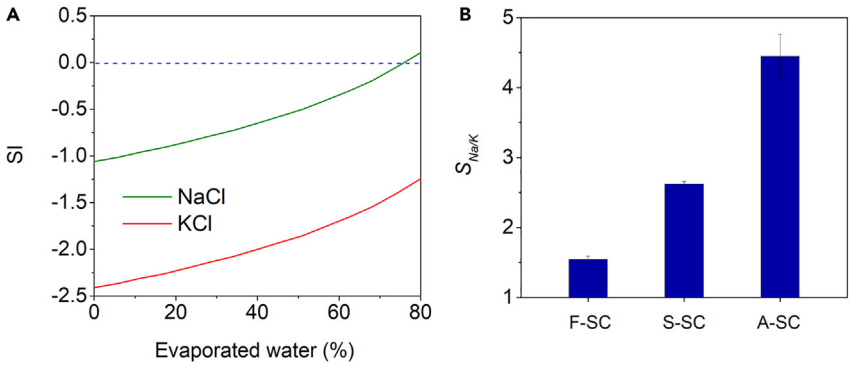

Figure 3. Ion-selective crystallization facilitated by SCs

(A) Simulated changes in saturation index (SI) of NaCl (green) and KCl (red) in a solution containing 10 wt % NaCl and 2 wt % KCl because of evaporation. The dotted line represents the solubility equilibrium, indicating the point at which the solution is saturated. Below the line, re-dissolution is preferred rather than crystallization.

(B) The selectivity of Na^+ to K^+ in the crystallized salt produced from the solution with F-SC, S-SC, and A-SC after 12 h of solar crystallization. Data are represented as mean ± SD.

crystallization process on the flat 2D SC was not much selective. In contrast, S-SC exhibited higher ion-selectivity ($S_{Na/K}$ = 2.62) than F-SC because the 3D structure of S-SC induced a Marangoni flow that facilitated solution flow than a conventional capillary flow.[36] The facilitated flow supplies more unsaturated solution to the crystallized salt and allows for re-dissolution and crystallization of the salt. Because the SI value of K^+ in the solution is lower than that of Na^+, the supplied solution dissolves K^+ more preferentially, leading to a relative increase in Na^+ in the crystallized salt.

It is worth noting that, although both S-SC and A-SC have identical 3D configurations in terms of surface area and height, A-SC exhibited significantly higher selectivity (4.45) than S-SC (2.62). The difference in ion-selectivity between A-SC and S-SC can be attributed to difference in solution transport because of their distinct mountain shapes. Although the mountains in S-SC have flat sides, those in A-SC have bent sides consisting of a series of consecutive V-shaped grooves, featuring one side that is convex and the other side that is concave (Scheme 1). When the sum of the water contact angle (θ) and the half-angle of the groove (α) is smaller than 90°, a rivulet can be formed on a V-shaped groove.[38,39] Because PPy-coated FP has a θ value of nearly 0 (Figure S5) and A-SC has an α value of 30°, a rivulet can form in the groove and allow additional solution transport, resulting in a higher solution transport.

Re-dissolution of salt by facilitated water transport through a rivulet

The water transport through a rivulet can be visualized by monitoring the diffusion of red dye in the mountain of A-SC. The red dye was selected to simulate the re-dissolution of salts because it consists of a mixture of water-soluble sodium salts (Amaranth ($C_{20}H_{11}N_2O_{10}S_3 \cdot 3Na$) and Sunset Yellow FCF ($C_{16}H_{10}N_2O_7S_2 \cdot 2Na$)). Figures 4A and 4B show the time-lapse optical images of S-SC and A-SC, respectively, with each SC spiked at the top with red dye powder placed on a wet FP. As water is transported from the bottom to the mountain of S-SC through capillary action, the powder dissolves and starts to diffuse. The color change of S-SC because of the diffusion is slow and limited near the top of the mountain for 20 min. However, an immediate color change appears along the V-shaped groove of A-SC, and the color change reaches the bottom within 1 min, indicating that the rivulet in the groove facilitated water transport. A control experiment was conducted using flat and V-shaped FP strips to observe the formation of a rivulet clearly. When one end of each strip was immersed in water, a rivulet formed in the V-shaped strip, resulting in more facilitated water transport because of the higher water volume in the rivulet compared to the pores inside the FP (Figure S6).

The water transport through a rivulet plays a key role in the re-dissolution and crystallization of the salt that forms along the mountain folds by increasing the contact between the crystallized salt and the solution. To demonstrate the influence of the rivulet on the ion-selective re-dissolution, equal amounts (20 mg) of KCl and NaCl salts were placed on S-SC and A-SC, and their dissolution was monitored during dark evaporation of a solution containing 10% NaCl and 2% KCl. Unlike solar evaporation, dark evaporation has a slower

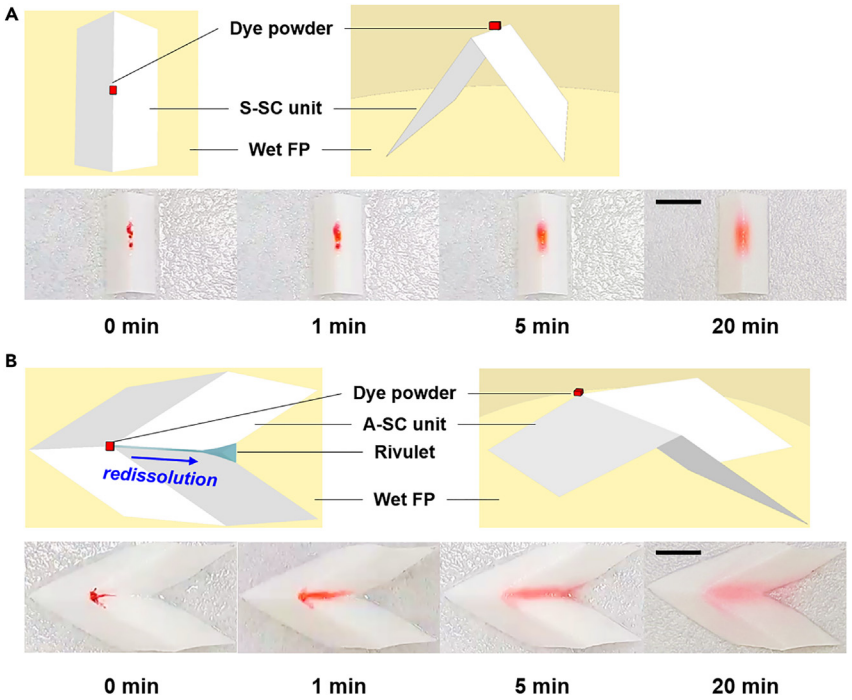

Figure 4. Dissolution of dye powder by facilitated water transport through a rivulet

Schematics and time-lapse optical images of (A) S-SC and (B) A-SC. Each SC was spiked with red dye powder at the top and placed on a wet FP. The scale bar represents 5 mm.

evaporation rate and promotes salt dissolution rather than crystallization. Figures 5A and 5B show time-lapse optical images of the KCl and NaCl salts on S-SC and A-SC, respectively. In both SCs, KCl dissolves faster than NaCl because the SI value of K^+ is lower than that of Na^+. Although nearly complete dissolution of the salts was observed for A-SC in ~3 h, it took >9 h for S-SC. The faster dissolution in A-SC was attributed to the formation of a rivulet, which facilitated additional solution transport and thereby resulted in higher transport efficiency.

Conclusions

In summary, we investigated the ion-selectivity of SCs for the first time and compared the performance of three SCs with different shapes: F-SC, S-SC, and A-SC. Although S-SC and A-SC have identical 3D configurations in terms of surface area and height, A-SC exhibited significantly higher ion-selectivity than S-SC, which was attributed to the V-shaped grooves present in A-SC that formed rivulets and facilitated water

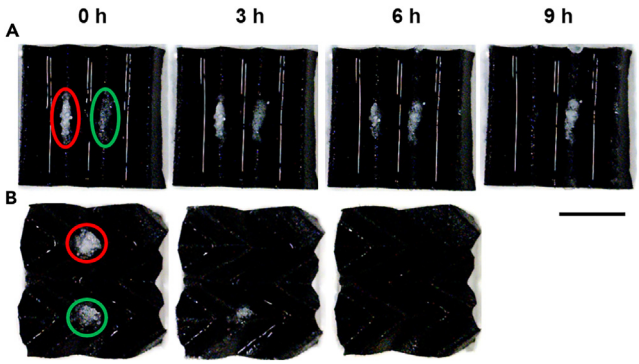

Figure 5. Re-dissolution of salts under dark evaporation

Time-lapse optical images of the KCl (red circle) and NaCl (green circle) salts on (A) S-SC and (B) A-SC during dark evaporation. The scale bar represents 10 mm.

transport to the crystallized salt. This allowed for re-dissolution and crystallization of the salt, leading to a higher ion-selectivity. When A-SC was employed to evaporate a solution containing a mixture of Na^+ and K^+ ions, the relative concentration of Na^+ to K^+ in the salt was 4.45 times higher than that in the initial solution (i.e., an ion-selectivity is 4.45), which is significantly higher than that achieved using F-SC (1.54) and S-SC (2.62). The high evaporation rate and ion-selectivity of A-SC make it a promising candidate to replace conventional brine mining processes.

LIMITATIONS OF THE STUDY

This study presents the high potential of A-SC for industrial application, specifically in brine mining processes, because of its high evaporation rate and ion-selectivity. However, certain limitations must be considered. Although the purity of the crystallized salt from A-SC was high (95%), it may still not be suitable for certain applications, necessitating additional purification processes. Furthermore, further investigation is required to understand the impacts of ion species and ratio on ion-selectivity. Although conventional brine mining processes are time-consuming, with bulk evaporation taking over a year, A-SC presents a viable alternative that could reduce process time and improve productivity. Nevertheless, additional research is required to address the aforementioned issues before A-SC can be adopted as a full-scale solution for brine mining.

STAR★METHODS

Detailed methods are provided in the online version of this paper and include the following:

- KEY RESOURCES TABLE
- RESOURCE AVAILABILITY
  - Lead contact
  - Materials availability
  - Data and code availability
- EXPERIMENTAL MODEL AND SUBJECT DETAILS
- METHOD DETAILS
  - Preparation of F-SC, S-SC, and A-SC
  - Evaporation performance of F-SC, S-SC, and A-SC
  - Ion-selectivity and saturation index (SI)
- QUANTIFICATION AND STATISTICAL ANALYSIS

SUPPLEMENTAL INFORMATION

Supplemental information can be found online at https://doi.org/10.1016/j.isci.2023.106926.

ACKNOWLEDGMENTS

This work was supported by the National Research Foundation of Korea (NRF) Grant funded by the Korea government (MSIT; No. 2019R1A5A8080290).

AUTHOR CONTRIBUTIONS

Conceptualization, J.C. and S.J.; Methodology, J.C. and S.J.; Investigation, J.C. and J.N.; Writing – Original draft, J.C. and S.J.; Writing – Review and Editing, J.C. and S.J.; Visualization, J.C.; Supervision, S.J.; Project Administration, S.J.; Funding Acquisition, S.J.

DECLARATION OF INTERESTS

The authors declare no competing interests.

Received: March 14, 2023
Revised: May 8, 2023
Accepted: May 16, 2023
Published: May 18, 2023

REFERENCES

1. Song, J.F., Nghiem, L.D., Li, X.-M., and He, T. (2017). Lithium extraction from Chinese salt-lake brines: opportunities, challenges, and future outlook. Environ. Sci. Water Res. Technol. *3*, 593–597. https://doi.org/10.1039/C7EW00020K.

2. Butts, D. (2003). Chemicals from brine. In Kirk-Othmer Encyclopedia of Chemical Technology (John Wiley & Sons, Inc.), pp. 784–803.

3. Loganathan, P., Naidu, G., and Vigneswaran, S. (2017). Mining valuable minerals from seawater: a critical review. Environ. Sci. Water Res. Technol. *3*, 37–53. https://doi.org/10.1039/C6EW00268D.

4. Kumar, A., Naidu, G., Fukuda, H., Du, F., Vigneswaran, S., Drioli, E., and Lienhard, J.H. (2021). Metals recovery from seawater desalination brines: technologies, opportunities, and challenges. ACS Sustain. Chem. Eng. *9*, 7704–7712. https://doi.org/10.1021/acssuschemeng.1c00785.

5. Sharkh, B.A., Al-Amoudi, A.A., Farooque, M., Fellows, C.M., Ihm, S., Lee, S., Li, S., and Voutchkov, N. (2022). Seawater desalination concentrate—a new Frontier for sustainable mining of valuable minerals. npj Clean Water *5*, 9. https://doi.org/10.1038/s41545-022-00153-6.

6. Nayar, K.G., Fernandes, J., McGovern, R.K., Dominguez, K.P., McCance, A., Al-Anzi, B.S., and Lienhard, J.H. (2019). Cost and energy requirements of hybrid RO and ED brine concentration systems for salt production. Desalination *456*, 97–120. https://doi.org/10.1016/j.desal.2018.11.018.

7. Ounissi, T., Dammak, L., Fauvarque, J.F., and Selmane Bel Hadj Hmida, E. (2021). Ecofriendly lithium-sodium separation by diffusion processes using lithium composite membrane. Separ. Purif. Technol. *275*, 119134. https://doi.org/10.1016/j.seppur.2021.119134.

8. Kim, J., Han, S.H., Kim, H.I., Cho, S.H., Choi, H., Kim, H.-Y., and Lee, Y.S. (2021). Interfacial solar evaporator - physical principles and fabrication methods. J. Surg. Oncol. *124*, 1347–1355. https://doi.org/10.1007/s40684-021-00337-4.

9. Tamimi, A., and Rawajfeh, K. (2007). Lumped modeling of solar-evaporative ponds charged from the water of the Dead Sea. Desalination *216*, 356–366. https://doi.org/10.1016/j.desal.2006.11.022.

10. Abdulsalam, A., Idris, A., Mohamed, T.A., and Ahsan, A. (2017). An integrated technique using solar and evaporation ponds for effective brine disposal management. Int. J. Sustain. Energy *36*, 914–925. https://doi.org/10.1080/14786451.2015.1135923.

11. Zeng, Y., Yao, J., Horri, B.A., Wang, K., Wu, Y., Li, D., and Wang, H. (2011). Solar evaporation enhancement using floating light-absorbing magnetic particles. Energy Environ. Sci. *4*, 4074–4078. https://doi.org/10.1039/C1EE01532J.

12. Ghasemi, H., Ni, G., Marconnet, A.M., Loomis, J., Yerci, S., Miljkovic, N., and Chen, G. (2014). Solar steam generation by heat localization. Nat. Commun. *5*, 4449. https://doi.org/10.1038/ncomms5449.

13. Wu, S.-L., Chen, H., Wang, H.-L., Chen, X., Yang, H.-C., and Darling, S.B. (2021). Solar-driven evaporators for water treatment: challenges and opportunities. Environ. Sci. Water Res. Technol. *7*, 24–39. https://doi.org/10.1039/D0EW00725K.

14. Choi, J., Lee, H., Sohn, B., Song, M., and Jeon, S. (2021). Highly efficient evaporative cooling by all-day water evaporation using hierarchically porous biomass. Sci. Rep. *11*, 16811. https://doi.org/10.1038/s41598-021-96303-w.

15. Xu, K., Wang, C., Li, Z., Wu, S., and Wang, J. (2021). Salt mitigation strategies of solar-driven interfacial desalination. Adv. Funct. Mater. *31*, 2007855. https://doi.org/10.1002/adfm.202007855.

16. Yan, L., Yang, X., Zhang, Y., Wu, Y., Cheng, Z., Darling, S.B., and Shao, L. (2021). Porous Janus materials with unique asymmetries and functionality. Mater. Today *51*, 626–647. https://doi.org/10.1016/j.mattod.2021.07.001.

17. Jang, H., Choi, J., Lee, H., and Jeon, S. (2020). Corrugated wood fabricated using laser-induced graphitization for salt-resistant solar steam generation. ACS Appl. Mater. Interfaces *12*, 30320–30327. https://doi.org/10.1021/acsami.0c05138.

18. Sohn, B., Song, M., Choi, J., and Jeon, S. (2022). Wood scrolls as highly efficient all-day steam generators. Adv. Sustain. Syst. *6*, 2200259. https://doi.org/10.1002/adsu.202200259.

19. Liu, H., Jin, R., Duan, S., Ju, Y., Wang, Z., Yang, K., Wang, B., Wang, B., Yao, Y., and Chen, F. (2021). Anisotropic evaporator with a T-shape design for high-performance solar-driven zero-liquid discharge. Small *17*, 2100969. https://doi.org/10.1002/smll.202100969.

20. Gu, R., Yu, Z., Sun, Y., Su, Y., Wu, W., and Cheng, S. (2022). Janus 3D solar crystallizer enabling an eco-friendly zero liquid discharge of high-salinity concentrated seawater with antiscalant. Desalination *537*, 115862. https://doi.org/10.1016/j.desal.2022.115862.

21. Wang, Y., Wu, X., Wu, P., Yu, H., Zhao, J., Yang, X., Li, Q., Zhang, Z., Zhang, D., Owens, G., and Xu, H. (2022). Salt isolation from waste brine enabled by interfacial solar evaporation with zero liquid discharge. J. Mater. Chem. A Mater. *10*, 14470–14478. https://doi.org/10.1039/D2TA03004G.

22. Zhang, C., Shi, Y., Shi, L., Li, H., Li, R., Hong, S., Zhuo, S., Zhang, T., and Wang, P. (2021). Designing a next generation solar crystallizer for real seawater brine treatment with zero liquid discharge. Nat. Commun. *12*, 998. https://doi.org/10.1038/s41467-021-21124-4.

23. Xia, Y., Hou, Q., Jubaer, H., Li, Y., Kang, Y., Yuan, S., Liu, H., Woo, M.W., Zhang, L., Gao, L., et al. (2019). Spatially isolating salt crystallisation from water evaporation for continuous solar steam generation and salt harvesting. Energy Environ. Sci. *12*, 1840–1847. https://doi.org/10.1039/C9EE00692C.

24. Mao, J., Li, J.-J., Xie, A.-Q., Liang, Y., Yang, Y., Zhu, L., and Chen, S. (2022). High-performance integrated solar steam generator for synergetic freshwater production, salt harvesting, and electricity generation. Solar RRL *6*, 2200330. https://doi.org/10.1002/solr.202200330.

25. Wang, W., Aleid, S., Shi, Y., Zhang, C., Li, R., Wu, M., Zhuo, S., and Wang, P. (2021). Integrated solar-driven PV cooling and seawater desalination with zero liquid discharge. Joule *5*, 1873–1887. https://doi.org/10.1016/j.joule.2021.05.010.

26. Ma, X., Jia, X., Yao, G., and Wen, D. (2022). Umbrella evaporator for continuous solar vapor generation and salt harvesting from seawater. Cell Rep. Phys. Sci. *3*, 100940. https://doi.org/10.1016/j.xcrp.2022.100940.

27. Hong, S., Shi, Y., Li, R., Zhang, C., Jin, Y., and Wang, P. (2018). Nature-inspired, 3D origami solar steam generator toward near full utilization of solar energy. ACS Appl. Mater. Interfaces *10*, 28517–28524. https://doi.org/10.1021/acsami.8b07150.

28. Wu, X., Wu, Z., Wang, Y., Gao, T., Li, Q., and Xu, H. (2021). All-cold evaporation under one sun with zero energy loss by using a heatsink inspired solar evaporator. Adv. Sci. *8*, 2002501. https://doi.org/10.1002/advs.202002501.

29. Xiao, J., Guo, Y., Luo, W., Wang, D., Zhong, S., Yue, Y., Han, C., Lv, R., Feng, J., Wang, J., et al. (2021). A scalable, cost-effective and salt-rejecting MoS2/SA@melamine foam for continuous solar steam generation. Nano Energy *87*, 106213. https://doi.org/10.1016/j.nanoen.2021.106213.

30. Gao, C., Zhu, J., Li, J., Zhou, B., Liu, X., Chen, Y., Zhang, Z., and Guo, J. (2022). Honeycomb-structured fabric with enhanced photothermal management and site-specific salt crystallization enables sustainable solar steam generation. J. Colloid Interface Sci. *619*, 322–330. https://doi.org/10.1016/j.jcis.2022.03.122.

31. Baspineiro, C.F., Franco, J., and Flexer, V. (2020). Potential water recovery during lithium mining from high salinity brines. Sci. Total Environ. *720*, 137523. https://doi.org/10.1016/j.scitotenv.2020.137523.

32. Na, C.-K., and Park, H. (2016). Recycling of waste bittern from salt farm (I) : recovery of magnesium. Appl. Chem. Eng. *27*, 427–432. https://doi.org/10.14478/ACE.2016.1058.

33. Chen, Y., Yang, J., Zhu, L., Wang, S., Jia, X., Li, Y., Shao, D., Feng, L., and Song, H. (2023). Marangoni-driven biomimetic salt secretion evaporator. Desalination *548*, 116287. https://doi.org/10.1016/j.desal.2022.116287.

34. Morciano, M., Fasano, M., Boriskina, S.V., Chiavazzo, E., and Asinari, P. (2020). Solar passive distiller with high productivity and Marangoni effect-driven salt rejection. Energy Environ. Sci. *13*, 3646–3655. https://doi.org/10.1039/D0EE01440K.

35. Zou, M., Zhang, Y., Cai, Z., Li, C., Sun, Z., Yu, C., Dong, Z., Wu, L., and Song, Y. (2021). 3D printing a biomimetic bridge-arch solar evaporator for eliminating salt accumulation with desalination and agricultural applications. Adv. Mater. *33*, 2102443. https://doi.org/10.1002/adma.202102443.

36. Shao, Y., Shen, A., Li, N., Yang, L., Tang, J., Zhi, H., Wang, D., and Xue, G. (2022). Marangoni effect drives salt crystallization away from the distillation zone for large-scale continuous solar passive desalination. ACS Appl. Mater. Interfaces *14*, 30324–30331. https://doi.org/10.1021/acsami.2c04572.

37. Kolthoff, I.M. (1932). Theory of coprecipitation. The formation and properties of crystalline precipitates. J. Phys. Chem. A *36*, 860–881. https://doi.org/10.1021/j150333a008.

38. Thammanna Gurumurthy, V., Rettenmaier, D., Roisman, I.V., Tropea, C., and Garoff, S. (2018). Computations of spontaneous rise of a rivulet in a corner of a vertical square capillary. Colloids Surf. A Physicochem. Eng. Asp. *544*, 118–126. https://doi.org/10.1016/j.colsurfa.2018.02.003.

39. Gerlach, F., Hussong, J., Roisman, I.V., and Tropea, C. (2020). Capillary rivulet rise in real-world corners. Colloids Surf. A Physicochem. Eng. Asp. *592*, 124530. https://doi.org/10.1016/j.colsurfa.2020.124530.

40. Monnin, C., and Ramboz, C. (1996). The anhydrite saturation index of the ponded brines and sediment pore waters of the Red Sea deeps. Chem. Geol. *127*, 141–159. https://doi.org/10.1016/0009-2541(95)00069-0.

41. Langmuir, D., and Melchior, D. (1985). The geochemistry of Ca, Sr, Ba and Ra sulfates in some deep brines from the Palo Duro Basin, Texas. Geochem. Cosmochim. Acta *49*, 2423–2432. https://doi.org/10.1016/0016-7037(85)90242-X.

42. Worch, E. (2015). Precipitation/dissolution equilibria. In Hydrochemistry (De Gruyter), pp. 110–118.

STAR★METHODS

KEY RESOURCES TABLE

REAGENT or RESOURCE	SOURCE	IDENTIFIER
Chemicals, peptides, and recombinant proteins		
Filter paper	Advantec	No.1
Sodium chloride	Samchun	S2097; CAS: 7647-14-5
Pyrrole	Sigma-Aldrich	131709; CAS: 109-97-7
Iron(III) chloride hexahydrate	Sigma-Aldrich	31232; CAS: 10025-77-1
Potassium chloride	Sigma-Aldrich	P3911; CAS: 7447-40-7
The red food dye (a mixture of Amaranth and Sunset Yellow FCF)	Chun-woo	CAS: 915-67-3, 2783-94-0
Other		
Deionized water system	Human Science	Human Power I^+
Ion chromatography	Thermo Scientific	Dionex Aquion
Scanning electron microscope	JEOL	JSM-7401F

RESOURCE AVAILABILITY

Lead contact

Further information and requests for resources should be directed to and will be fulfilled by the Lead Contact, Sangmin Jeon (jeons@postech.ac.kr).

Materials availability

This study did not generate new unique reagents.

Data and code availability

- All data reported in this paper will be shared by the lead contact upon request.
- This paper does not report original code.
- Any additional information required to reanalyze the data reported in this paper is available from the lead contact upon request.

EXPERIMENTAL MODEL AND SUBJECT DETAILS

This study does not use experimental models.

METHOD DETAILS

Preparation of F-SC, S-SC, and A-SC

Filter papers (FPs) were coated with polypyrrole (PPy) through *in situ* polymerization. The process involved immersing the FP in a 20 mL solution of 0.12 M pyrrole, followed by adding a 20 mL solution of 0.15 M iron(-III) chloride and polymerizing in ambient conditions for 15 min before quenching in DI water. The PPy-coated FP was cut into a 2 cm × 2 cm square shape to create F-SC, with an overall area and projected area of 4 cm^2. In contrast, S-SC and A-SC were created by folding a PPy-coated FP, resulting in an overall area of 8 cm^2 and a projected area of 4 cm^2 for both SCs. To ensure a constant supply of the solution, each SC was placed on a desk-shaped FP wick that was submerged in the solution. Scheme 1 shows the experimental setup and the schematic of each SC.

Evaporation performance of F-SC, S-SC, and A-SC

After placing each SC in a 20 mL water container, mass change in water during evaporation was measured using an electronic balance (AS220.R2, Radwag, Poland) and surface temperature was monitored with an IR camera (FLIR A315, FLIR Systems, Inc., OR, USA). A solar simulator (94011A, Newport, CA, USA) was used for uniform illumination, and the light intensity was measured with an optical power meter (1919-R,

Newport, CA, USA). Evaporation rate was calculated by dividing the change in water mass for 1 h by the projected area (4 cm^2). DI water was used for evaporation rate measurement, and a solution containing 10 wt% NaCl and 2 wt% KCl was used for solar crystallization. All experiments were conducted at a temperature of 26.5 $\pm$ 1.0 °C and a relative humidity of 18 $\pm$ 2%.

Ion-selectivity and saturation index (SI)

The ion concentration of the solution and the composition of the crystallized salt were determined using ion chromatography (Dionex Aquion, Thermo Scientific, MA, USA). Ion-selectivity ($S_{Na/K}$) was calculated using Equation 1, where R_{salt} and $R_{solution}$ are the mass ratio of Na^+ ion to K^+ ion in the crystallized salt and initial solution, respectively.

$$S_{Na/K} = \frac{R_{salt}}{R_{solution}} \quad \text{(Equation 1)}$$

The saturation index (SI) is used to predict whether a salt will crystallize or dissolve in a solution.[40] SI can be calculated by comparing the ion activity product (Q) of the salt in solution to its solubility product constant (Ksp),[41]

$$SI = \log\left(\frac{Q}{K_{sp}}\right) \quad \text{(Equation 2)}$$

where Ksp of NaCl and KCl are 37.7 and 20.8, respectively, at room temperature. A positive SI value indicates that the concentration of salt in the solution is higher than its solubility, and as a result, the salt is thermodynamically favorable to crystallize.[42]

QUANTIFICATION AND STATISTICAL ANALYSIS

The error bars in Figures 1, 2, 3, and S4 represent the standard deviation (SD) obtained using three independent measurements.